Pattern Recognition Letters 72 (2016) 100–108

Contents lists available at ScienceDirect

Pattern Recognition Letters

journal homepage: www.elsevier.com/locate/patrec

Understanding pollen tube growth dynamics using the Unscented Kalman Filter☆

Asongu L. Tambo[a,*], Bir Bhanu[a], Nolan Ung[b], Ninad Thakoor[a], Nan Luo[b], Zhenbiao Yang[b]

[a] Department of Electrical and Computer Engineering, Center for Research in Intelligent Systems, USA
[b] Department of Botany and Plant Sciences, University of California at Riverside, Riverside, CA 92521, USA

ARTICLE INFO

Article history:
Available online 4 August 2015

Keywords:
Pollen tubes
Apical growth
Tip growth
Mathematical model of tip growth

ABSTRACT

In the process of pollination, a pollen tube grows from a pollen grain that has fallen on the stigma of a flower. This tube grows towards the ovary of the flower where it will deliver male reproductive material. Knowledge of the dynamics of pollen tube growth will provide a basis for understanding more complex cells that exhibit similar growth behavior. Current pollen tube growth models are a collection of differential equations that represent the level of understanding that biologists have concerning apical growth. Due to their complex nature, these models are not used to verify observed behavior in living cells as seen under a microscope. We present a model that can be used to describe the behavior of growing pollen tube cells in actual experiments. We propose biologically relevant functions based on knowledge of the growth process to explain the dynamics of model parameters. Our model uses an affine transformation to propagate the tip of the cell and statistical parameter estimation to measure necessary parameters during growth. Using experimental videos of pollen tube growth, we show that our model can adapt to various growth scenarios while extracting growth parameters from the videos.

1. Introduction

Sexual reproduction in flowering plants produces seeds that ensure the continuation of the plant life cycle. This process is initiated by pollination: the transfer of pollen grains from the male part of the flower (anther) to the female part of the flower (stigma). The pollen tube grows from the grain into the style of the flower, navigating female tissue to deliver sperm for fertilization (Fig. 1). Unlike most cells, the pollen tube grows through polar extension wherein cell membrane and cell wall expansion is limited to the apical/tip region of the cell. To prevent the cell from bursting, new cell wall material is deposited at the growth site. The cycle of growth/deposition continues until the cell tip reaches the ovary where it bursts and fertilization occurs. Biologists study these processes to identify key ingredients and their functions. Mathematical models are an important tool in this study because they are able to measure and make predictions on how the shape of the cell evolves throughout the growth/deposition cycles. In the development of these tools, engineers/mathematicians require knowledge of the various pathways leading to cell growth as understood by the biologists.

Pollen tube growth oscillates between periods of activity and inactivity. When plant cells grow, they absorb water and increase the flexibility of their cell walls, allowing for expansion followed by reinforcement of those same cell walls ([22]). Tip growth is the result of two key systems: the first system provides a balance of forces between internal pressure (Turgor, Osmotic) and the stiffness of the cell wall resisting deformation. The second system deals with internal protein and ion dynamics that lead to the deposition of material at the growth site ([5,23]) by vesicles. Callose is a cell wall component that adds structure and flexibility that is selectively deposited in the shank providing rigidity to the cell wall while its absence in the tip provides a flexible domain that can flex and grow ([8]). In a slightly more complicated mechanism, pectin is deposited throughout all regions of the tube, however it exists in a *soft* form at the apex and transitions to a *hard* form as the shank forms through the action of enzymes that promote the pectin molecules to bind to each other. This binding creates a dense matrix that provides both the rigidity and plasticity needed for proper pollen tube growth ([16]). The transportation of material is facilitated by a network of dynamic cable-like fibers (F-actin network) that act as tracks on which vesicles travel and is highly responsive to the active cytosolic gradient of free calcium concentrated at the tip ([24]). Furthermore, the influx of intracellular calcium oscillates with pollen tube growth showing a spike in influx a few seconds after the burst of growth most likely promoting the rest phase ([11]).

☆ This paper has been recommended for acceptance by Anders Heyden.

* Corresponding author. Tel.: +1 9518273954.
E-mail address: atamb001@ucr.edu (A.L. Tambo).

http://dx.doi.org/10.1016/j.patrec.2015.07.016
0167-8655/

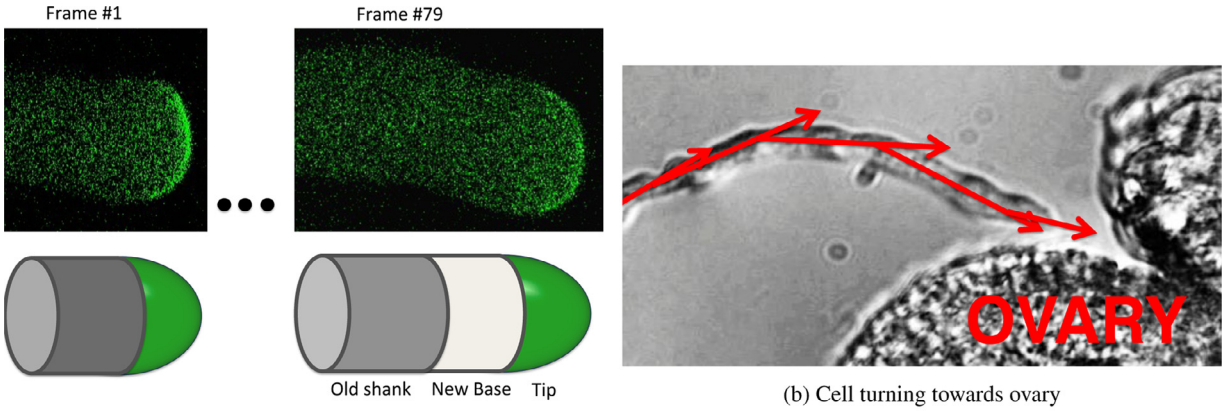

(a) Sample images and their corresponding representations using a standard model

(b) Cell turning towards ovary

Fig. 1. (a) Fluorescence images of a growing pollen tube from an experimental video with accompanying 3D rendition. (b) Enhanced bright field image of a pollen tube cell turning towards the ovary. Arrows show changes in tip orientation over time.

These dynamic processes are highly regulated and connected to one another through signaling cross talk by way of known and unknown mechanisms. Fig. 2 shows an artist's rendition of the components involved in the regulation of tip growth in pollen tubes. These known biological phenomena can then be used to inform mathematical models giving biologists a tool to predict the response to changes in the biological system and better design hypothesis and experiments.

In this paper, we discuss a mathematical model for the growth of pollen tubes as witnessed in experimental videos. We explicitly model those biological process that are observable in the videos, and make meaningful assumptions of other underlying processes that are not observable. In the following sections, we summarize current mathematical models of tip growth in Section 2. Section 3 covers the theoretical development of the proposed method including assumptions made about the growth process. Section 4 covers experimental results and discussion of these results, and Section 5 presents the conclusions of the paper.

2. Related work and contributions

2.1. Related work

There are many factors that affect the growth of pollen tubes, some of which are ion concentrations (e.g. K^+, Ca^{2+}, H^+, Cl^-), turgor pressure and osmotic pressure. The net result of the interactions between these agents is a change in the cell size (i.e. increase in cell length and volume). The complex nature of apical growth has been addressed by a few models in recent literature: ([3,7,10,14,17]). Each model explains pollen tube growth by proposing differential equations to represent what is known about some aspects of the growth process. These models can be divided into two classes based on their area of focus: internal dynamics vs. cell wall dynamics.

Hill et al. [10] approach cell growth as the result of changing osmotic pressure when water from the surrounding enters the cell and causes swelling. This influx is caused by changes in ion concentrations within the cell which establishes an osmotic pressure gradient. Simulations of their model show similar growth (change in volume) patterns as those of *in vitro* pollen tubes. Since the pollen tube can be divided into two main parts: a hemispherical tip and a cylindrical shank (Fig. 1), [17] develop an integrated and self-regulatory two-compartment model whose ion dynamics lead to cell growth. Ion transporters connect these compartments to each other and the surrounding media. In this model, cell growth is the change in tip and shank volumes which are related to the dynamics of K^+, Ca^{2+}, H^+ and Cl^-) through a power law formalization of the cell growth rate.

Unlike the previous two models that focused mainly on internal dynamics, [3] present a model that focuses more on cell wall dynamics. The cell wall is modeled as an inhomogeneous viscous fluid shell

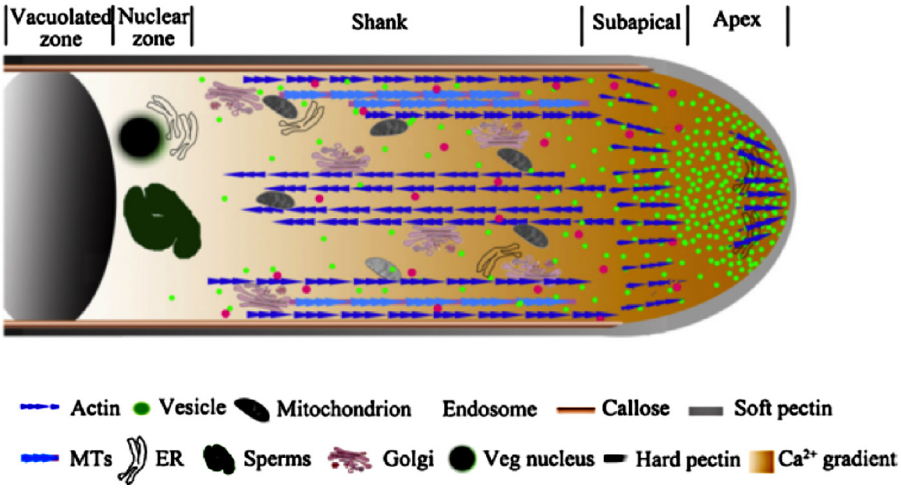

Fig. 2. Artists rendition taken from [21] of the cytoplasm of a pollen tube including cytoplasmic contents. Vesicles are produced from the golgi bodies and then make their way to the cell tip via actin filaments. The filaments indicate direction of vesicle traffic.

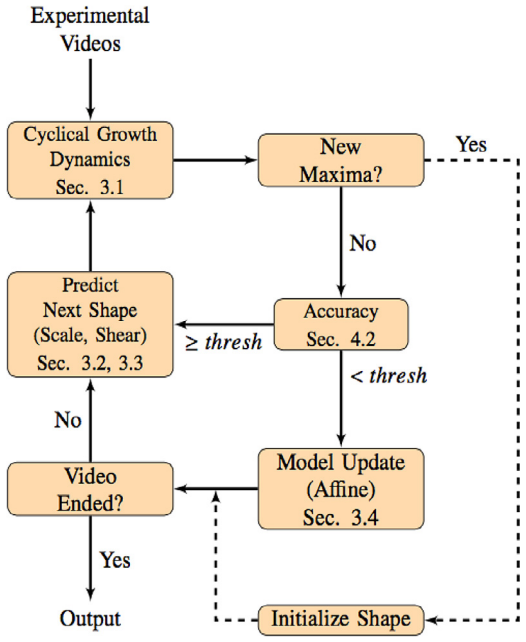

Fig. 3. Block diagram of the video analysis method. Images from a video are analyzed sequentially to get cell shape and tip fluorescence. When membrane fluorescence reaches a maximum, a new growth cycle begins. During each cycle, shape prediction is performed. Shape correction occurs when the error between predicted and measured shape exceeds a defined threshold.

that undergoes deformation due to internal turgor pressure. Material deposition at the deformation site, which is the result of internal dynamics, maintains cell wall thickness. In similar fashion, [7] consider the cell wall to be a thin shell of viscoplastic anisotropic composition. The stress-strain relationship between the cell wall and turgor pressure is expressed following the Lockahrt equation ([18]) for elastic materials.

2.2. Contributions of this paper

While the above models account for cell growth using different approaches, the common thread is the lack of experimental validation of their models using video evidence. Furthermore, some of the key parameters required by these models cannot be measured/observed in experimental videos. In our previous work ([25]), we presented a model for deforming the cell tip using an affine transformation. Here, we advance that model by making the following contributions: (1) an adaptive model for deforming the tip of a growing pollen tube according to experimental evidence; (2) a statistical method for online estimation of model parameters required to grow the observed tip; (3) validation of our model using experimental data. Using biologically relevant functions for the shape parameters, we show online estimation of model parameters using the Unscented Kalman Filter. The estimated parameter values, together with model assumptions, validate that the component of Turgor pressure in the growth direction (elongation) is greater than the component that causes the cell tip to expand.

3. Technical approach

In this section, we present the technical approach of our method. Fig. 3 lists the main parts of our method in a block diagram. Given an experimental video of a growing pollen tube, we extract the average fluorescence (f_{avg}) along the cell wall over time (cyclical growth dynamics). Maxima in f_{avg} indicate the start of a new growth cycle, and the current cell tip shape becomes the initial shape. The system then enters a prediction-correction loop until either the video ends, or a new maxima is detected in f_{avg}. The system output is a list of model parameters, shapes and shape accuracies for each detected growth cycle.

3.1. Model building using biology of pollen tube growth

The basic representation of the pollen tube consists of a cylindrical *shank* that is the main body of the cell, and a hemispherical *tip* that is the apical region. Cell growth is restricted to the apical region, except in some cases of cell turning where part of the cylindrical body is also extended. This turning is brought about by the weakening and stretching of the cell wall at the growth region ([9]). This stretching leads to thinning of the cell wall and cell membrane and would otherwise lead to cell bursting without the deposition of growth material by vesicles during exocytosis ([19]). This deposition is cyclical and produces cyclical growth patterns ([11]). To avoid an increase or decrease in cell wall thickness, the rate of deposition should be close to the rate of wall thinning. A higher rate of deposition will increase wall thickness while a lower rate would not keep up with wall thinning. As such, we consider that the rate of vesicle fusion (material deposition) is equal to the rate of cell wall reconstruction during exocytosis. Vesicles are produced within the cytoplasm and conveyed to the growth region ([2]). Deposited vesicles form an *inverted cone* shape with the base being the region of growth. To best describe the amount of accumulated vesicles in this zone, we use a Gaussian distribution centered at the middle of the growth region (maximum) and tapers towards the subapical region (Fig. 2).

Given the resolution of the experimental videos in this study, it is not possible to detect vesicles. Pollen tubes from the plant *Arabidopsis Thaliana* have an average tube diameter of 5 μm ([4]) and mean vesicle diameter of 0.182 μm ([13]). Given an average image resolution of 0.0582 μm/pixel, the expected size of the pollen tube is 86 pixels and 3 pixels for a vesicle, which makes vesicle detection very challenging. Since individual vesicles cannot be tracked, we need a secondary means to determine the location where vesicles will congregate. The active form of the protein ROP1 has been shown to be an important regulator of tip growth ([21,27]) by promoting the construction of the F-actin network used to convey vesicles to the growth region. By monitoring green fluorescence protein (GFP)-tagged RIP1 protein, we can determine the localization of active ROP1 along the cell membrane, and consequently the site of vesicle deposition. The combined volume of the deposited vesicles is the amount of new wall material needed for growth. But it is not possible to determine the number of deposited vesicles due to the resolution of the images. As such, we consider the strength of the fluorescence signal to be proportional to the number of deposited vesicles, since this signal helps to build the network on which these vesicles travel.

3.2. Detailed model development

Consider $X = \{[x_i, y_i]^T, i = 1, \ldots, N\}$ as the set of N-2D points along the tip of the tube in the image plane, and that the cell is elongating vertically. For any two given sets of points: $X(t)$ and $X(t + \Delta t)$, the following relationship can be established:

$$X(t+\Delta t) = \begin{bmatrix} a(t) & 0 \\ 0 & b(t) \end{bmatrix} \begin{bmatrix} 1 & c(t) \\ 0 & 1 \end{bmatrix} X(t) \tag{1}$$

where Δt is the sampling time, $a(t)$ and $b(t)$ are scaling parameters (strain) in the horizontal and vertical directions respectively, and $c(t)$ is a shear parameter that controls tip turning and determines the growth direction and orientation of the cell tip (Fig. 4). The two matrices in Eq. (1) are scale and shear matrices. Eq. (1) holds for any two time points. Knowing a suitable equation for the dynamics of the affine parameters is crucial in predicting the shape of the growing cell. We define each growth parameter according to the functions:

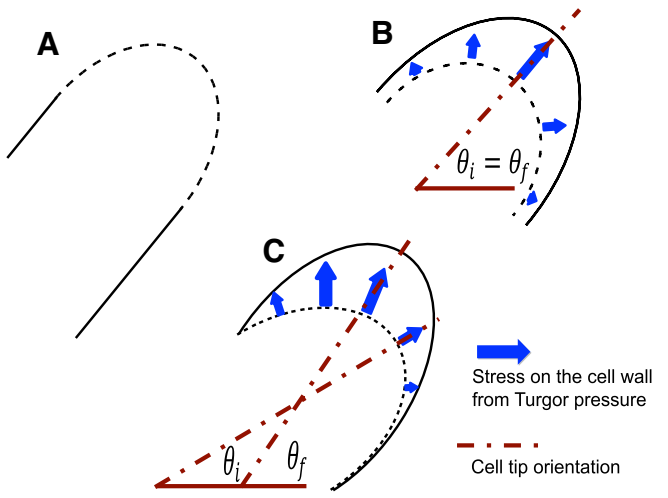

Fig. 4. (A) 2D rendition of pollen tube cell with cell tip (dashed) and shank. (B) Cell tip deforming through elongation and expansion. Initial(θ_i) and final (θ_f) tip orientations are the same. (C) Cell tip turning. Initial tip orientation is not the same as the final tip orientation.

$$a(t) = 1 + a'\Delta t \tag{2a}$$

$$b(t) = 1 + b'\Delta t \tag{2b}$$

$$c(t) = f\left(\theta_f, \theta_i, u\right) \tag{2c}$$

where a' and b' are the cell wall strain rates in the horizontal and vertical directions respectively, (θ_i, θ_f) are the initial and final cell orientations respectively, and u is the rate of cell turning.

Growth of the pollen tube is the result of stretching cell wall fibers (without breaking them). The relationship between the strain rate ($\dot{\epsilon}$) and the stress on the cell wall due to internal turgor pressure, P:[Newton per sq. Meter], is not a novel problem in the study of cell growth mechanics ([7,18]). This relationship, $\dot{\epsilon} = \Phi(P - P_{osmotic})$, says that cell growth can only occur if $(P - P_{osmotic}) = 0$ (for a constant extensibility Φ). [15] have shown that there is very minimal change in turgor pressure within the cell. We, therefore, adopt the premise that growth is the result of a weakening cell wall, not excess pressure:

$$\frac{\partial}{\partial t}\epsilon = P\frac{\partial}{\partial t}(\psi) \tag{3}$$

where Ψ:[sq. Meters per Newton] is the inverse of the elastic modulus of the cell wall fibers. Ψ is affected by the deposition of material during exocytosis. For a suitable function to capture cell wall weakening, we suggest the use of the the Gompertz logistic function.

$$\frac{\partial}{\partial t}\psi = r\psi ln\left(\frac{K}{\psi}\right) \tag{4}$$

where r:[per second] is the rate of vesicle fusion (material deposition) and K:[sq. Meters per Newton] is the maximum attainable weakness in the cell wall (when the cell wall is weakest without bursting).

This adoption is based on the understanding of the biological processes that lead to cell wall weakening (Section 1), and a history of modeling population growth. Just as the growth of a species depends on available resources and the consumption rate, stable pollen tube growth can be described as the consumption of deposited material to build new cell wall and ensure that the cell does not rupture. This function allows for asymptotic growth behavior observed at:

1. *Start of a growth cycle*: This is the start of material deposition when vesicles start fusing with the cell membrane. The cell wall is made up of mostly hard pectin. As more material is deposited, the rate of conversion of hard-to-soft pectin gradually increases.
2. *End of a growth cycle*: This marks the end of exocytosis when a majority of vesicles have already fused with the cell membrane. During this phase, material deposition for wall reconstruction is reducing. As such, the rate of conversion of soft-to-hard pectin gradually reduces, and growth slows down since the cell tip is hardening.

Combining Eq. (2)–(4) gives:

$$\frac{\partial}{\partial t}a = P_a r a ln\left(\frac{K}{a}\right) \tag{5a}$$

$$\frac{\partial}{\partial t}b = P_b r b ln\left(\frac{K}{b}\right) \tag{5b}$$

where $P_{(\bullet)}$ denotes the component of turgor pressure in the specified direction.

The effects of the parameter $c(t)$ are most noticeable when the cell is turning. In such cases, the dynamics of $c(t)$ determines how the orientation of the cell changes over time. *To the best of our knowledge, there have been no previous quantitative studies on the mechanism(s) of cell turning.* Without sufficient data on pollen tube turning, it is not possible to assign a particular function that controls tube turning i.e. Is tube turning a linear, polynomial, exponential, etc. function, and what are its dependencies? To determine the dynamics of turning, we use the generalized logistic function:

$$c(t) = \theta_i + \frac{\theta_f - \theta_i}{(1 + \nu \cdot exp\{-u(t - t_m)\})^{1/\nu}} \tag{6}$$

where (θ_i, θ_f: [*rads*]) are the initial and final orientations of the cell respectively, u [s^{-1}] is the rate of cell turning, ν depends on the initial orientation, and t_m marks the time at which cell turning is maximum. Our choice of this function is based on its flexibility to adapt to various cell turning scenarios.

Eqs. (1), (2), (5) and (6) are sufficient to explain the deformation of the growth region for any two time points. The behavior of the deformation depends on the parameters of the deformation functions. Since no two growth cycles are similar, these growth parameters are expected to change and must be determined for each growth cycle.

3.3. Online estimation of model parameters

Estimating the appropriate parameters for the growth equation leads to correct predictions about the position of the cell tip over time while analyzing an experimental video. We employ two schemes for estimating the affine transform parameters that determine shape evolution. For the shear parameter (c), we use a simple scheme to estimate its values over time. At a given time t, the value of the transform parameters depend on the current value in the prediction array and the previous 3 values in the measurement-array. The prediction array ($\hat{c}$) is a history of the values used in the transformation, and the measurement array ($\tilde{c}$) is a history of the transformation values between two consecutive observations of the cell tip. The shear parameter (c) is predicted using:

$$\hat{c}'(t+1) = 0.5\left(\hat{c}'(t) + \frac{1}{3}\sum_{i=max([0,\ t-2])}^{t}\tilde{c}'(t)\right) \tag{7}$$

Post-fitting of Eq. (6) to the measured data supports the choice of a logistic equation for the transformation parameters.

For parameters a and b, whose evolution is guided by Eq. (4), we use the Unscented Kalman Filter (UKF) developed by [12]. The Kalman Filter is a statistical tool for determining the states of a dynamic system in the presence of noise. It employs a prediction-correction loop to modify both the state predictions and the covariance matrix that indicates the "confidence" in the predictions. As more samples are

observed, the filter states should converge to the actual states (governed by the state equations) and the variation in the covariance matrix should stabilize. In our application, we wish to estimate both the states and the parameters involved in the state transitions of Eq. (4). This type of estimation (of both the states and the parameters) is referred to as *joint* estimation ([26]). Since the first-order Taylor series expansion of Eq. (4) is also nonlinear, the UKF is ideal for estimating the dynamics of Eq. (4). Note that a UKF-estimation is performed for each of the affine parameters a and b with separate state vectors: $\mathbf{x}_a$ and $\mathbf{x}_b$.

Let $\mathbf{x}_a = [a, a', r_a, K_a]^T$ and $\mathbf{x}_b = [b, b', r_b, K_b]^T$ be the augmented state vectors that define the affine parameters controlling expansion and elongation, respectively. $\mathbf{x}_{(\bullet)}$ evolves according to the following state and measurement equations:

$$\mathbf{x}_\zeta(t+\Delta t) = \begin{bmatrix} 1 & \Delta t & 0 & 0 \\ & f(\zeta, r, K) & & \\ 0 & 0 & 1 & 0 \\ 0 & 0 & 0 & 1 \end{bmatrix} \mathbf{x}_\zeta(t) + \mathbf{v}(t) \tag{8a}$$

$$y(t+\Delta t) = \begin{bmatrix} 0 & 1 & 0 & 0 \end{bmatrix} \mathbf{x}_\zeta(t) + \mathbf{w}(t) \tag{8b}$$

where $\zeta = (a, b)$, $f(.)$ is defined in Eq. (4), $\mathbf{v}$, and $\mathbf{w}$ are zero-mean Gaussian random variables denoting the system and measurement variances, respectively.

3.4. Online shape correction

As with all prediction tasks, the expected shape does not always match the observation. This section discusses techniques for reconciling the predicted tip shape and the observed shape obtained via image segmentation. These techniques are employed when the prediction accuracy falls bellow a user-specified threshold. In our experiments, this threshold is: $acc_{thresh} = 0.9$. Section 4.2 outlines the metric used in determining shape accuracy. To best describe the process of error correction, consider that at a given time, $t = i$ with a given shape P_i, a prediction is made for the shape at the next time interval $t = j$, $j > i$ denoted by P_j. At $t = j$ the observed shape O_j is recorded. If the accuracy between the prediction P_j and the observation O_j falls bellow the specified threshold, the following steps are taken to correct the prediction:

1. Since we know the previous shape P_i and the current observation O_j, we determine the affine parameters for deforming the shape from $P_i \rightarrow O_j$ in the Least-squares sense:

$$(\hat{a}, \hat{b}, \hat{c}) = arg \min_{a,b,c} \sum_{k=1}^{N} ||O_j(k) - \begin{bmatrix} \hat{A} & \hat{T} \\ 0 & 1 \end{bmatrix} P_i(k)|| \tag{9}$$

   where $\hat{A}$ is a (2×2) matrix and $\hat{T}$ is a (2×1) translation vector, and N is the number of 2D points in P_i.
2. Using a combination of QR-decomposition and factorization, $\bar{A}$ is decomposed into rotation, scale, and shear matrices:

$$\hat{A} = \begin{bmatrix} p & -q \\ q & p \end{bmatrix} \begin{bmatrix} \hat{a} & 0 \\ 0 & \hat{b} \end{bmatrix} \begin{bmatrix} 1 & \hat{c} \\ 0 & 1 \end{bmatrix} \tag{10}$$

   where $(\hat{a}, \hat{b}, \hat{c})$ are the update values for the affine matrix parameters. Since the type of shape deformation involved in tip growth does not require rotations, the influence of the rotation matrix is considered as noise and not used in updating the shape.
3. The updated shear parameter and predicted shape P_i become:

$$c(i-1) \leftarrow \hat{c} \tag{11a}$$

$$P_j \leftarrow \hat{A} O_i + \hat{T}, \tag{11b}$$

   $\hat{A}$ and $\hat{T}$ are obtained in Eq. (9). Affine parameters a and b are updated separately in UKF update process.

Algorithm 1 outlines the steps for online analysis of a fluorescent video of a growing pollen tube.

4. Experiments

4.1. Experimental setup and data collection

In this study, pollen tubes were grown from pollen grains taken from the plant Arabidopsis Thalinia. This plant serves as a model organism for the study of pollen tube growth because its entire genome is known. Green fluorescent protein (GFP) was fused to Arabidopsis RIP1 (AT1G17140, also named ICR1) on the C-terminus. This served as a marker of active ROP1. The RIP1-GFP fragment was fused into a binary vector pLat52::NOS, which contains a pollen tube specific promoter, to generate the binary construct pLat52::RIP1-GFP construct. Using Agrobacterium mediated flower dip method, pLat52::RIP1-GFP was introduced into Arabidopsis wild-type Col0 background. Arabidopsis thaliana plants were grown at 22°C in growth rooms under a light regime of 16 h of light and 8 h of dark. Pollen grains were germinated on a solid medium (18% sucrose, 0.01% boric acid, 1 mM (milli Molar) CaCl2, 1 mM Ca(NO3)2, 1 mM MgSO4, pH 6.4 and 0.5% agar) for 3 hours before observation under a microscope. Pollen tubes expressing GFP-ROP1, GFP-RIC1, GFP-RIC4 or RLK-GFP were observed using a Leica SP2 confocal microscope (488nm excitation, 500–540 nm emission). Images of the median plane of the pollen tube were obtained as time-lapse images using a confocal microscope. The response of pollen tubes to external stimulus was observed using a modified semi in-vitro assay as described by [20].

For each video used in this study, Table 1 shows the microscope acquisition rate, the number of images in the video, the spacing between successive analyzed images, and the total number of analyzed images. The first few frames [3–6] of each sequence are used to establish the first growth cycle, and no predictions are recorded for the fist frame in each growth cycle (initialization). For example, in Fig. 5, the first 6 frames are used to establish the first cycle, and there are a total of 6 growth cycles. Hence $119 - 6 - 6 = 107$ analyzed images.

Algorithm 1 Algorithm Pseudo-code.

```
Require: F: fluorescent video of growing pollen tube
Require: a_thresh: accuracy threshold for shape update
  while videoTerminated == false do
    I ← getnextframe(F)
    C ← contour of segmented pollen tube
    S ← append{S, mean(I(C))}
    Sm ← maxima turning points in S
    if isNotEmpty(Sm) then
      if isNewMaxima( Sm(end) ) then
        Xi ← (x, y) : C(x, y) = brightest cell contour region
        Initialize parameter states: (x_a, x_b, c)
        Initialize Covariance matrices: P_a, P_b
        Xpred ← predict next shape: (1), (2), (8)
      else
        A ← accuracy of prediction: (12)
        if A < a_thresh then
          Update shape: (9)–(11)
        end if
        Update UKF states and matrices
        Xi ← Predict next shape: (1), (2), (8)
      end if
    end if
  end while
```

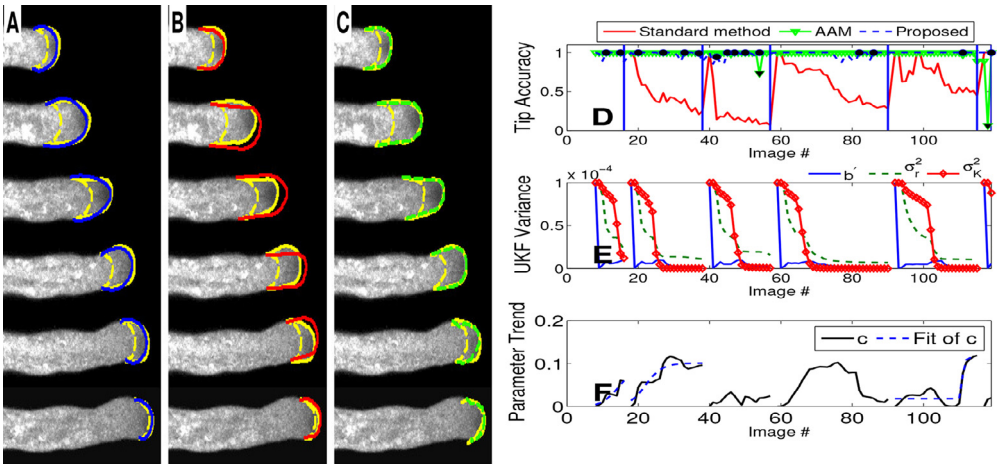

Fig. 5. Results of tip tracking in a video showing straight growth with 6 detected growth cycles. (A) The proposed method (blue) as deformed from the starting position (yellow) to match the observed tip. (B) Standard method of adding cylinders at the base of the tip (red). (C) Results of AAM (green) in tip localization. (D) Accuracy of the three methods over time. Shaded circles indicate when model was corrected and shaded squares indicate when the AAM was updated. (E) Variance in parameters for elongation reduces during online parameter estimation with UKF. (F) Cumulative sum of variation in the shear parameter (c) over time. Fit not shown when the R-squared-value is below 0.85. (For interpretation of the references to colour in this figure legend, the reader is referred to the web version of this article).

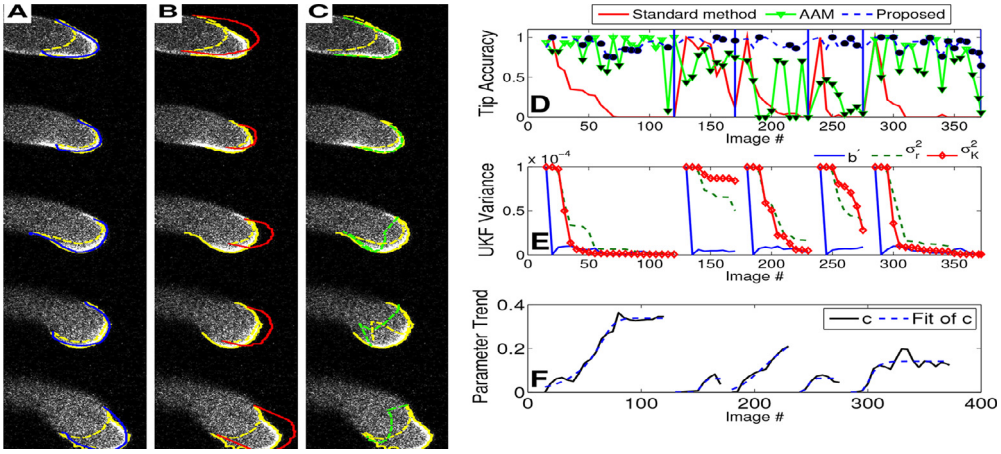

Fig. 6. Results of tip tracking on a video showing tube turning with 5 detected growth cycles. (A) The proposed method (blue) as deformed from the starting position (yellow) to match the observed tip. (B) Adding cylinders at the base of the tip (red) is not sufficient to explain tip turning. (C) Results of AAM (green) in tip localization. (D) Accuracy of the three methods over time. Shaded circles indicate when model was corrected and shaded triangles indicate when the AAM was updated. (E) Variance in parameters for elongation reduce during online parameter estimation with UKF. (F) Cumulative sum of variation in the shear parameter over time. (For interpretation of the references to colour in this figure legend, the reader is referred to the web version of this article).

Table 1
Acquisition rate (χ), video length (l), analysis spacing (Δt) and number of images analyzed for each experimental video.

Property	Figure number						
	5	6	7 a	7 b	7 c	7 d	7 e
Acquisition rate	0.1	1.0	0.5	1.0	1.0	0.1	1.0
Video length	119	372	93	252	79	119	294
Spacing	1	5	3	5	2	2	5
Number of analyzed images	107	69	26	46	66	107	55

4.2. Accuracy metric

The accuracy of the predicted shape of the cell tip is determined on a pixel-by-pixel basis. An accurate pixel is one that is within a distance of n-pixels from the observed tip contour (O). The accuracy of the predicted tip contour (P) is determined using the following metric:

$$Accuracy_{pixel}(P, O) = \frac{sum(d)}{length(P)} \tag{12}$$

where

$$d(i) = \begin{cases} 1 & \text{if } min(||P_i - O||) \leq n \\ 0 & \text{Otherwise} \end{cases} \tag{13}$$

for $i = 1, \ldots, length(P)$, and $||.||$ is the L_2 norm. We use a distance of $n = 3$ pixels in our analysis.

4.3. Experimental results

In this section, we show the results of our method (this paper) and compare it with the standard method of adding cylinders to the base of the tip for pollen tube growth as well as adaptive active appearance model (AAM)([1,6]) on experimental videos. The AAM was trained by manually indicating the tip region on the training images. When detection accuracy fell bellow 0.85, the AAM was updated by using the manually-drawn tip on the current image as a new training example.

Fig. 5 shows the results of the proposed method in analyzing a video of a pollen tube exhibiting straight growth. There are 119 images in the sequence with a 10-second gap between each image. This spacing provides sufficient gap between consecutive images. 107 out

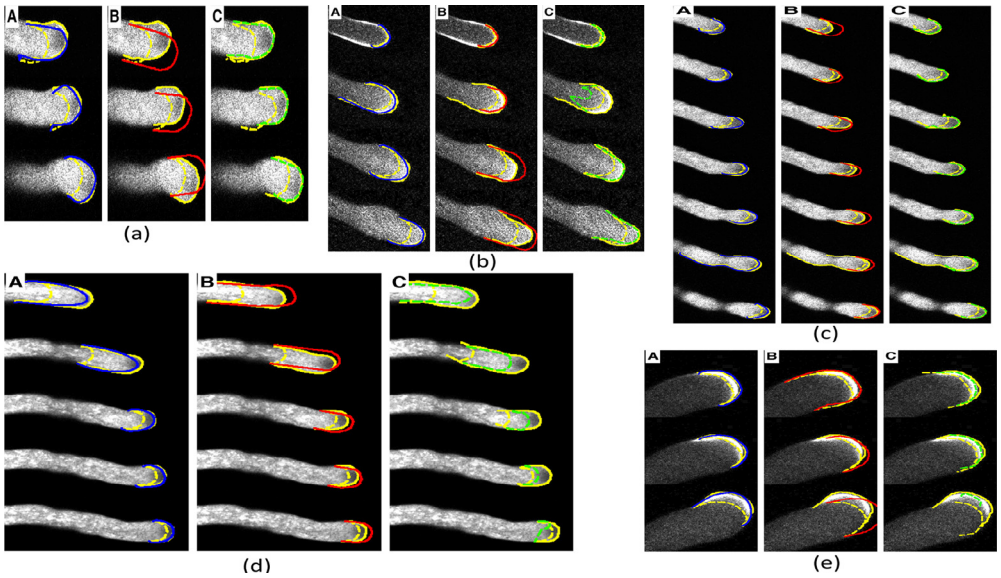

Fig. 7. Results of the proposed method on different videos of pollen tube growth vs. the standard approach and AAM for tip detection. [Blue]: proposed method, [Red]: standard method, [Green]: AAM, [Yellow]: observed tip. (For interpretation of the references to colour in this figure legend, the reader is referred to the web version of this article).

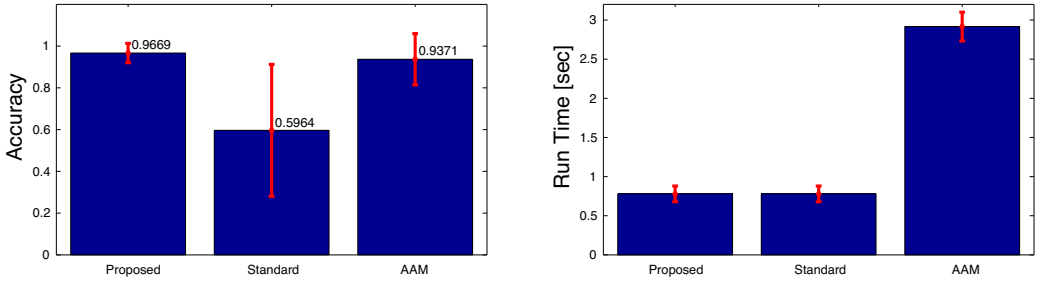

(a) Accuracy statistics (b) Run time statistics

Fig. 8. Mean (bars) and standard deviation (error bars) of accuracy and runtime of the three methods used in the experiments shown in Fig. 7. In (a), the numbers indicate the mean accuracy for each method.

of 119 images were analyzed. 6 growth cycles were detected, as represented by the 6 rows of images show in A, B, and C. Fig. 5A shows the deformation of the initial shape (yellow) at the end of the growth cycle (blue) according to the proposed method, Fig. 5B shows the result of the standard approach of adding cylinders to the base of the tip (red), and Fig. 5C shows the result of tip detection using AAM (green). Fig. 5D shows the accuracy of the three methods over time for each of the 6 growth cycles. Growth cycles are separated by vertical lines. During the entire experiment, 5 shape corrections were performed for the proposed model compared to 4 for AAM. These correction times are indicated by filled circle and triangle-markers on the accuracy curves respectively and were performed when accuracy fell bellow 85%. Fig. 5E indicates that during the course UKF-estimation, the variance of the states (not showing the first state: position) decreases over time. This signals a convergence of the estimated parameters. The last plot shows a fit of Eq. (7) to the cumulative sum of the shear parameter (c) during each growth cycle. The fit is not shown if the accuracy falls below 85%.

Similarly, Fig. 6 shows the results on a video of a pollen tube that is turning towards the ovary. The microscope acquisition rate was 1 *image*/*s*. To allow for significant variation between two consecutive shapes, we select every 5th image in the sequence for a total of 69 analyzed images out of 372. Unlike in the previous case, this example has a lot of variation in the shape of the tip during the course of the experiment. Fig. 6A indicates that the proposed method can adapt to the observations as the tip first turns down, then slightly to the right in the last cycle. This rich dynamic is missed by the standard method (Fig. 6B) because of its rigid nature. AAM-based detection is not always able to detect the tip in the image. This is more evident in the corresponding accuracy plot (green) of Fig. 6D, compared with the accuracy of the proposed method (blue). Similar to Figs. 5E, 5F, 6E, 6F show the decrease in variance over time, and the fit of Eq. (7) to the dynamics of the shear parameter over each growth cycle.

The above two experiments are presented as examples to show the flexibility of the proposed method in adapting to changing tip deformations. Even though Eqs. (4) and (7) are not used in the experimental analysis, they are capable of explaining the observed data and can, therefore, be used in theoretical studies. These experiments also show that with proper training, AAMs can be used for tip detection but not as a predictor of tip localization, which is what the proposed method does. The strength of our method is evident in that it is able to adapt to various tip representations (turning, bulging, straight growth), as well as cases with some registration problems between the start and end of the growth cycle.

Figs. 7 and 8 summarize the results of 5 experiments comparing the proposed method (Column A) to standard pollen tube growth (Column B) and AAM (Column C). These experiments contain a total of 317 analyzed images. Since AAMs capture both shape and

Table 2
Mean and standard deviation of the results from parameter estimation during curve evolution shown in the indicated figures.

Figure number	Expansion (a)		Elongation (b)		$\frac{P_b r}{P_a r}$
	P_ar	K $\times 10^{-3}$	P_br	K $\times 10^{-3}$	
5	0.0611 ± 0.0127	0.1263 ± 0.0934	0.1042 ± 0.0218	0.1986 ± 0.2104	1.7047
6	0.0296 ± 0.0077	0.1932 ± 0.0706	0.0328 ± 0.0092	0.2678 ± 0.0943	1.1073
7 a	0.0619 ± 0.0057	0.0632 ± 0.0452	0.0938 ± 0.0115	0.20918 ± 0.0338	1.5147
7 b	0.0288 ± 0.0081	0.1515 ± 0.0348	0.0279 ± 0.0149	0.2528 ± 0.0879	0.9643
7 c	0.0536 ± 0.0133	0.2097 ± 0.0956	0.0809 ± 0.0310	0.2334 ± 0.1244	1.5094
7 d	0.0339 ± 0.0140	0.2212 ± 0.1635	0.0519 ± 0.0348	0.6304 ± 0.6896	1.5315
7 e	0.0150 ± 0.0022	0.1330 ± 0.0176	0.0238 ± 0.0080	0.3074 ± 0.0563	1.5898

appearance information, they work best when neither the shape nor the appearance (pixel intensity distribution) of the tip changes dramatically. There are some exceptions as shown in column C of Fig. 7(d) where the appearance of the intensity distribution at the tip drops and contributes to false tip localization. AAMs were set to run for 25 iterations, which had an average runtime of 2.92 seconds. The proposed method is approximately 4-times faster with a higher average accuracy as indicated in Fig. 8.

Table 2 shows the mean and standard deviation of the parameters estimated using UKF for the indicated experiments. Since pollen tubes grow principally through elongation and we make no distinction between cell wall fibers stretching in both direction, we expect the value of $P_b r$ to be higher than that of $P_a r$ (Table 2, Column 6). This is because P_a is expanding pressure while P_b is the elongating pressure. In Fig. 7(b), the tip of the cell becomes wider towards the end of the second cycle, indicating a higher than normal expanding pressure (P_a) during this cycle.

5. Conclusions

We have presented a method for growing a pollen tube cell that is based on an interpretation of the underlying biological activity, as well as a deformation of the growth region that is located around the tip of the cell. Cell deformation is a mechanical process governed by the balance between internal pressure and wall stiffness. We model cell growth as result of the reduction in wall stiffness (reduction in wall viscosity) caused by the deposition of material during exocytosis. We use the periodic nature of exocytosis, linked to oscillations of cytosolic Ca^{2+}, to initialize our model at the start of each growth period. We have shown that the dynamics of cell wall weakening can be explained using a Gompertz logistic function. Since this function is nonlinear, we employed the Unscented Kalman Filter in estimating function parameters during each growth cycle. Our experimental results showed that affine transformations can be used to grow the cell tip to the desired shape, and that the dynamics of the affine parameters satisfy the proposed logistic growth model.

The adaptive model presented works both in cases of straight growth as well as during tube turning. In each case, the model is able to detect the beginning of each growth cycle, enabling it to reinitialize model parameters to reflect this biological signal. Statistical online parameter estimation is used to determine the parameters of the model during each growth cycle, with no training involved. To the best of our knowledge, the authors are not aware of any work that applies a model for apical pollen tube growth directly to an experimental video. As such, this work would be instrumental as the first step in quantifying the many parameters involved in apical growth.

Acknowledgment

This work is funded by NSF Grant *DGE 0903667* to Dr. Bhanu as the PI and Tambo (as NSF IGERT Fellow), and National Institute of General Medical Sciencesgrant (*R01GM100130*) to Dr. Yang.

Supplementary material

Supplementary material associated with this article can be found, in the online version, at doi:http://dx.doi.org/10.1016/j.patrec.2015.07.016.

References

[1] A.U. Batur, M.H. Hayes, Adaptive active appearance models., IEEE Trans. Image Process. 14 (11) (2005) 1707–1721.
[2] J. Bove, B. Vaillancourt, J. Kroeger, P.K. Hepler, P.W. Wiseman, A. Geitmann, Magnitude and direction of vesicle dynamics in growing pollen tubes using Spatiotemporal image correlation Spectroscopy and fluorescence recovery after photobleaching., Plant Phys. 147 (4) (2008) 1646–1658, doi:10.1104/pp.108.120212.
[3] O. Campàs, L. Mahadevan, Shape and dynamics of tip-growing cells., Curr. Biol. 19 (24) (2009) 2102–2107, doi:10.1016/j.cub.2009.10.075.
[4] Y. Chebli, M. Kaneda, R. Zerzour, A. Geitmann, The cell wall of the Arabidopsis pollen tube-spatial distribution, recycling, and network formation of polysaccharides., Plant Phys. 160 (4) (2012) 1940–1955, doi:10.1104/pp.112.199729.
[5] R.a. Cole, J.E. Fowler, Polarized growth: maintaining focus on the tip., Curr. Opin. Plant Biol. 9 (6) (2006) 579–588, doi:10.1016/j.pbi.2006.09.014.
[6] T.F. Cootes, C.J. Taylor, An algorithm for tuning an active appearance model to new data, Proceedings of the British Machine Vision Conference 2006 (2006) 94.1–94.10, doi:10.5244/C.20.94.
[7] J. Dumais, S.L. Shaw, C.R. Steele, S.R. Long, P.M. Ray, An Anisotropic-Viscoplastic model of plant cell Morphogenesis by tip growth., Int. J. Dev. Biol. 50 (2-3) (2006) 209–222, doi:10.1387/ijdb.052066jd.
[8] C. Ferguson, T. Teeri, M. Siika-Aho, S. Read, A. Bacic, Location of cellulose and callose in pollen tubes and grains of Nicotiana Tabacum, Planta 61 (1998) 452–460.
[9] P.K. Hepler, C.M. Rounds, L.J. Winship, Control of cell wall extensibility during pollen tube growth., Mol. Plant 6 (4) (2013) 998–1017, doi:10.1093/mp/sst103.
[10] A.E. Hill, B. Shachar-hill, J.N. Skepper, J. Powell, Y. Shachar-hill, An Osmotic model of the growing pollen tube, PLoS ONE 7 (5) (2012) e36585, doi:10.1371/journal.pone.0036585.
[11] T. Holdaway-Clarke, J. Feijo, Pollen tube growth and the intracellular Cytosolic calcium gradient oscillate in phase while extracellular calcium influx is delayed, Plant Cell 9 (November 1997) (1997) 1999–2010.
[12] S. Julier, J. Uhlmann, A New Extension of the Kalman Filter to Nonlinear Systems, Proceedings of the AeroSense: The 11th International Symposium on Aerospace/Defense Sensing, Simulation and Control. (1997).
[13] T. Ketelaar, M. Galway, B. Mulder, A. Emons, Rates of exocytosis and endocytosis in Arabidopsis root hairs, J. Microsc. 231 (Pt 2) (2008) 265–273.
[14] J.H. Kroeger, A. Geitmann, M. Grant, Model for calcium dependent Oscillatory growth in pollen tubes., J. Theor. Biol. 253 (2) (2008) 363–374, doi:10.1016/j.jtbi.2008.02.042.
[15] J.H. Kroeger, R. Zerzour, A. Geitmann, Regulator or driving force? The role of Turgor pressure in Oscillatory plant cell growth., PLoS ONE 6 (4) (2011) e18549, doi:10.1371/journal.pone.0018549.
[16] Y. Li, F. Chen, H. Linskens, M. Cresti, Distribution of unesterified and esterified Pectins in cell walls of pollen tubes of flowering plants, Sex. Plant Reprod. 7 (3) (1994) 145–152.
[17] J. Liu, B.M.A.G. Piette, M.J. Deeks, V.E. Franklin-Tong, P.J. Hussey, A compartmental model analysis of integrative and self-regulatory ion dynamics in pollen tube growth., PLoS ONE 5 (10) (2010) e13157, doi:10.1371/journal.pone.0013157.
[18] J.A. Lockhart, An analysis of irreversible plant cell elongation., J. Theor. Biol. 8 (2) (1965) 264–275.
[19] S.T. McKenna, J.G. Kunkel, M. Bosch, C.M. Rounds, L. Vidali, L.J. Winship, P.K. Hepler, Exocytosis precedes and predicts the increase in growth in oscillating pollen tubes., Plant Cell 21 (10) (2009) 3026–3040, doi:10.1105/tpc.109.069260.
[20] R. Palanivelu, D. Preuss, Distinct short-range ovule signals attract or repel Arabidopsis Thaliana pollen tubes in vitro., BMC Pant Biol. 6 (2006) 7, doi:10.1186/1471-2229-6-7.
[21] Y. Qin, Z. Yang, Rapid tip growth: Insights from pollen tubes., Semin. Cell Dev. Biol. 22 (8) (2011) 816–824, doi:10.1016/j.semcdb.2011.06.004.

[22] D. Rayle, R. Cleland, The acid growth theory of Auxin-induced cell elongation is alive and well, Plant Phys. 99 (4) (1992) 1271–1274.
[23] J. Samaj, J. Müller, M. Beck, N. Böhm, D. Menzel, Vesicular Trafficking, Cytoskeleton and signalling in root hairs and pollen tubes., Trends Plant Sci. 11 (12) (2006) 594–600, doi:10.1016/j.tplants.2006.10.002.
[24] L. Steinhorst, J. Kudla, Calcium - a central regulator of pollen germination and tube growth., Biochimica et Biophysica Acta 1833 (7) (2013) 1573–1581, doi:10.1016/j.bbamcr.2012.10.009.
[25] A. Tambo, B. Bhanu, N. Luo, G. Harlow, Z. Yang, Integrated model for understanding pollen tube growth in video, in: 22nd International Conference on Pattern Recognition (ICPR) 2014, 2014, pp. 2727–2732.
[26] E. Wan, R.V.D. Merwe, The Unscented Kalman filter for nonlinear estimation, IEEE Adaptive Systems For Signal Processing, . Communications, and Control Symposium (2000) 153–158.
[27] Z. Yang, Cell polarity signaling in Arabidopsis, Annu. Rev. Cell Dev. Biol. 24 (2008) 551–575, doi:10.1146/annurev.cellbio.23.090506.123233.Cell.